Journal of Materials Chemistry A

COMMUNICATION

View Article Online
View Journal | View Issue

Cite this: J. Mater. Chem. A, 2018, 6, 18821

Received 27th May 2018
Accepted 31st August 2018

DOI: 10.1039/c8ta04959a

rsc.li/materials-a

Self-adaptive electrochemical reconstruction boosted exceptional Li^+ ion storage in a Cu_3P@C anode†

Shibing Ni,*[ab] Bin Zheng,[a] Jilei Liu,[b] Dongliang Chao,[b] Xuelin Yang,[a] Zexiang Shen*[b] and Jinbao Zhao[c]

Self-adaptive electrochemical reconstruction is proven to trigger superior performance of conversion anode materials for Li-ion batteries. In the case of Cu_3P, Cu_3P dots embedded in a carbon matrix resulting in high Li-ion storage activity, improved electronic conductivity and stability is induced and results in an ultralong (>10 000 cycles) lifespan.

While the performance of conversion anode materials has been significantly improved since their first utilization in Li-ion batteries (LIBs) in 2000,[1] the fundamental understanding of the underlying mechanisms that affect the performance is still limited. For instance, it was generally accepted that morphology destruction from cycling leads to a loss of electronic conductivity and activity of the electrode, which is regarded as the principal culprit for performance degradation.[2] Following this, three main strategies have focused on improving the structural stability of the conversion type anodes *via* initial structure design: (1) nano-sized morphology design;[3–8] (2) hybridization with carbonaceous materials;[9–14] and (3) freestanding electrode construction.[15–20] Despite the significant progress achieved, the understanding of the key factors that affect the performance of conversion anodes is not keeping pace with the improvement in performance. Up to now, insufficient emphasis has been placed on dealing with the morphology evolution of conversion anodes in cycling and the related electrochemical properties to clarify the underlying mechanisms associated with their intrinsic performance.

Herein, we try to address these challenges to some extent by tracking the morphology variation of conversion anodes through *ex situ* SEM, TEM, selected area electron diffraction (SAED) and HRTEM, and assessing the morphology related reaction kinetics. To demonstrate the validity of this attempt, Cu_3P, a specific conversion anode with suitable energy density and safety properties (Fig. S1†) but a moderate lifespan (<100 cycles),[21–32] was selected as a model. Following this, a unique architecture of Cu_3P@C directly grown on copper foam was firstly prepared (Fig. 1). During the fabrication, the *in situ* carbonization of C and phosphorization of Cu resulted in the formation of Cu_3P@C with homogeneous hybridization between Cu_3P and C at the nanoscale. SEM, TEM, SAED and HRTEM analysis revealed that the Cu_3P@C gradually transformed into, and stabilized as, a secondary architecture of Cu_3P dots embedded in a C matrix through a well coordinated morphology evolution between Cu_3P and C. This was accompanied by the disassembly of Cu_3P agglomerations into small crystals and the spread of C nanoflake networks among the Cu_3P crystals. Such morphology evolution can be called electrochemical reconstruction, and it is this electrochemical reconstruction that gives the self-adaptive high reaction activity, electronic conductivity and stability, triggering improved

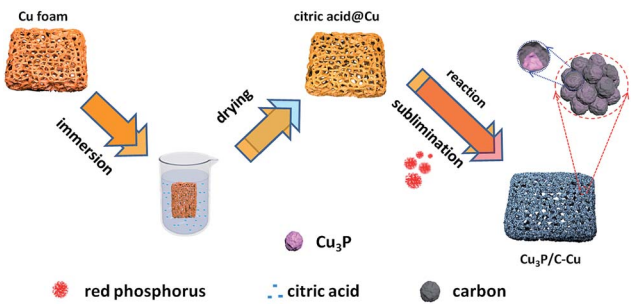

Fig. 1 Schematic diagram for the formation of the Cu_3P@C on Cu foam.

[a]College of Materials and Chemical Engineering, Hubei Provincial Collaborative Innovation Center for New Energy Microgrid, Key Laboratory of Inorganic Nonmetallic Crystalline and Energy Conversion Materials, China Three Gorges University, Yichang, 443002, China. E-mail: shibingni07@126.com

[b]School of Physical and Mathematical Sciences, Nanyang Technological University, 637371, Singapore. E-mail: zexiang@ntu.edu.sg

[c]State Key Laboratory of Physical Chemistry of Solid Surfaces, Collaborative Innovation Center of Chemistry for Energy Materials, State-Province Joint Engineering Laboratory of Power Source, Technology for New Energy Vehicle, College of Chemistry and Chemical Engineering, Xiamen University, Xiamen, Fujian, P. R. China

† Electronic supplementary information (ESI) available. See DOI: 10.1039/c8ta04959a

performance. As a result, the Cu_3P@C exhibits no capacity fading over 500 cycles at 0.15 A g^{-1} and excellent high-rate performance (270 mA h g^{-1} after 10 000 cycles at 4.2 A g^{-1}), which to the best of our knowledge is among the best for all reported Cu_3P electrodes. Triggering the performance of the conversion anode *via* the electrochemical reconstruction reported here provides new understanding of the inner mechanisms that affect the performance of conversion anodes, which is also valuable for electrode design.

Synthesis and structural characterization

The preparation of Cu_3P@C was realized *via* a facile one-step reaction. As shown in Fig. 1, citric acid molecules homogeneously absorb on the surface of the Cu foam during the immersion process. The carbonization of citric acid molecules and the phosphorization of Cu occur simultaneously during the sintering process with red P. The Cu_3P nanocrystals can promote the *in situ* carbonization of citric acid on their surface, forming the Cu_3P@C composite. The as-formed carbon can prevent the build-up of Cu_3P nanocrystals and improve the electronic conductivity of the composite (for the EIS spectra of Cu_3P@C–Cu and Cu_3P–Cu see Fig. S2†). As a result, the Cu_3P@C composite with homogeneous hybridization between Cu_3P and C can grow directly on Cu foam.

All the diffraction peaks in Fig. 2a match well with cubic Cu (JCPDS, no. 04-0836) and hexagonal Cu_3P (JCPDS, no. 65-3628). Futhermore, the existence of C in the Cu_3P@C composite is also confirmed by the Raman spectra in Fig. 2b, with a weight ratio of ~1.6% (Fig. S3†). The two peaks at 1378.8 and 1597.7 cm^{-1} can be attributed to the D-band and G-band of carbon.[32–35] Fig. 2c is the high resolution XPS spectrum of Cu 2p for the Cu_3P@C. The two peaks centered at 933.2 and 952.9 eV can be attributed to the Cu $2p_{3/2}$ and Cu $2p_{1/2}$ of Cu_3P. The high resolution XPS spectrum of P 2p for the Cu_3P@C is shown in Fig. 2d, in which the peaks at 128.3, 129.5 and 134.1 eV correspond to P $2p_{3/2}$ and P $2p_{1/2}$ for Cu_3P, and the oxidation state of P for the surface species.[36–38] The two peaks at 284.8 and 288.3 eV for the C 1s spectrum (Fig. 2e) can be assigned to the C–C bond of SP^3 spin–orbit levels of graphite-like C and O–C=O chemical bonds.[39,40] XPS results further confirm that the Cu_3P@C composite is successfully prepared, but it should be noted that long-term air exposure will lead to surface oxidation of the Cu_3P@C–Cu (for the XPS spectrum of Cu, P and O see Fig. S4†).[36,38,41,42] The SEM images in Fig. 2f and g suggest that the Cu_3P@C has a uniform film-like morphology, consisting of numerous embedded particles ranging from 20 to 500 nm with a homogeneous distribution of Cu, P and C (Fig. 2h). In contrast, the intrinsic Cu foam exhibits a smooth surface with distinct crystal boundaries (see the inset of Fig. 2g). The TEM images in Fig. 2i and j indicate that the Cu_3P@C consists of numerous particles ranging from tens of nanometers to ~1 μm, and these micro-particles are composed of primary nano-sized Cu_3P@C particles. The microstructure of the Cu_3P@C was also studied *via* SAED and HRTEM. The crystallized Cu_3P can be confirmed *via* the SAED pattern (Fig. 2k), while the imperfect distribution of diffraction spots indicates an irregular arrangement and uneven size distribution of the Cu_3P crystals. The HRTEM image in Fig. 2l exhibits clear fringes with an interplanar spacing of 0.22 nm (see the inset), corresponding to the (121) plane of hexagonal Cu_3P. A partial amorphous region stems from carbon that is well coated on the surface of Cu_3P. The preliminary FFT pattern (Fig. 2m) derived from the HRTEM image also displays the crystallographic planes of Cu_3P.

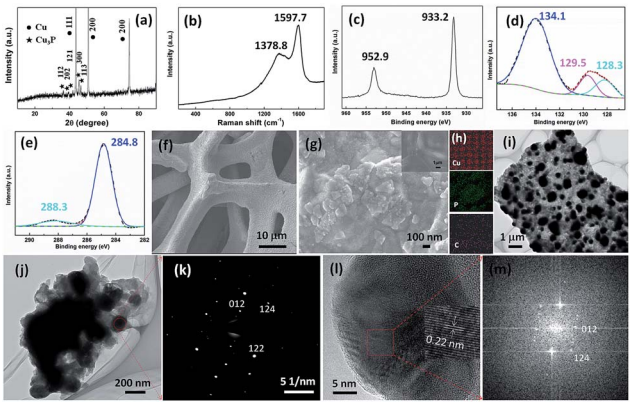

Fig. 2 Compositional and morphological information of the as-prepared sample. (a) XRD pattern, (b) Raman spectrum, (c) the high resolution XPS spectra of Cu 2p, (d) P 2p, (e) and C 1s. SEM images with low (f) and high (g) magnification. (h) EDS mapping images, TEM images with low (i) and high (j) magnification. (k) SAED pattern, (l) HRTEM image and (m) FFT pattern. The inset of (l) shows the corresponding lattice fringes.

Electrochemical reconstruction

To understand the inner mechanisms that correlate with the performance of the Cu_3P@C, *ex situ* TEM, HRTEM and SAED images displayed in Fig. 3 track the microstructural evolution of

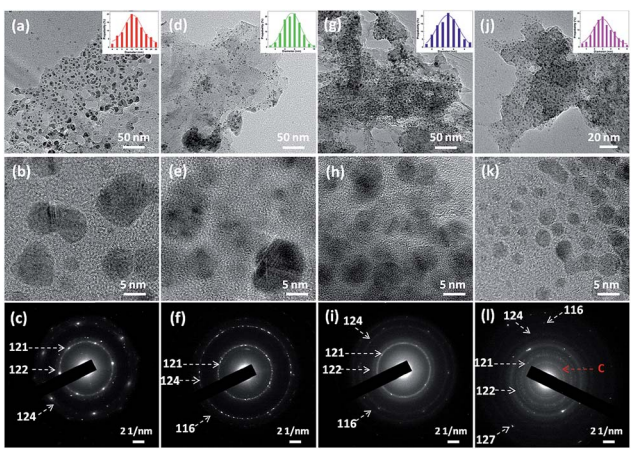

Fig. 3 (a), (d), (g) and (j) TEM; (b), (e), (h) and (k) HRTEM images; and (c), (f), (i) and (l) SAED patterns of the Cu_3P@C after different cycles. (a), (b) and (c) are after 1 cycle; (d), (e) and (f) are after 5 cycles; (g), (h) and (i) are after 10 cycles; (j), (k) and (l) are after 500 cycles.

the electrode with cycling. As shown in Fig. 3a and b, the Cu_3P@C after 1 cycle shows dots embedded in the matrix (D-in-M) architecture with a mean dot size of 12 nm. Also, the typical SAED pattern in Fig. 3c exhibits both regular diffraction spots and dispersive spots distributed as rings, suggesting the reduction of the Cu_3P particle size in the 1st cycle. In the subsequent cycles, a similar architecture of the Cu_3P@C is preserved, whereas the size of the Cu_3P particles continues to diminish. As shown in Fig. 3d and e, the Cu_3P@C after 5 cycles exhibits a mean dot size of ~5.5 nm. Such refinement of the Cu_3P dots is in accordance with the evolution of the SAED pattern shown in Fig. 3c–f. After that, the microstructure of the Cu_3P@C gradually reaches its stable state. As seen in Fig. 3g, h, j and k, the mean size of the Cu_3P dots decreases a little from 5 to 3 nm along with the increase of cycle numbers from 10 to 500 cycles. Such microstructure variation of the Cu_3P@C is in agreement with the SAED patterns in Fig. 3i and l, where new crystallographic planes of Cu_3P and C gradually appear upon cycling. Noticeably, even after 500 cycles, the integrity of the whole electrode is well sustained (Fig. S5†), though numerous nano-sized holes generate in the integral Cu_3P@C.

According to the morphological and microstructural evolution of the Cu_3P@C, the electrochemical reconstruction process can be presented (Fig. 4). The stress imposed upon lithiation/delithiation triggers the pulverization of aggregated Cu_3P particles accompanied by more coated carbon being exposed, forming unique composites with smaller Cu_3P dots well embedded into carbon matrix (Cu_3P@C D-in-M).[43] In the subsequent cycles, the D-in-M architecture is preserved, and the size of the Cu_3P dots continues to decrease (~5.5 nm after 5 cycles) and gradually tends towards stability (~5 nm) after 10 cycles. Such microstructure variation of the Cu_3P@C upon cycling is driven by the electrochemical reaction kinetics and is primarily due to: (1) the mechanical stability of the Cu_3P dots during lithiation/delithiation increases as the dot size reduces, which is similar to Si which displays negligible mechanical pulverization below a certain critical size (~5 nm);[44] (2) the carbon matrix can also well accommodate the stress generated by lithiation/delithiation on Cu_3P owing to its flexibility. In the D-in-M architecture, the small size of the Cu_3P dots gives high reaction activity and the embedded structure promotes high electron transfer efficiency, both of which are self-adaptive properties to trigger improved performance.

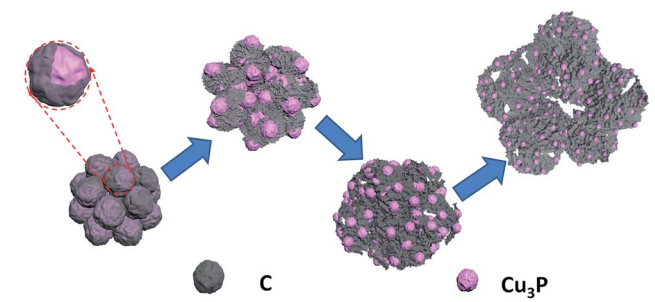

Fig. 4 Schematic of electrochemical reconstruction for the Cu_3P@C.

Electrochemical performance assessment

Based on the self-adaptive electrochemical reconstruction of the Cu_3P@C in cycling, the electrochemical performance of the Cu_3P@C–Cu electrode (~0.7 mg cm^{-2}) was evaluated. The CV curves were tested over a voltage region of 0–3.0 V at a scan rate of 0.2 mV s^{-1}. As shown in Fig. 5a, both CV curves show similar profiles, except for an extra reduction peak in the first cathodic scan near 1.44 V which is associated with side reactions (*i.e.*, decomposition of the electrolyte and the reduction of CuO).[21] Two reduction peaks near 0.63 and 0.82 V in the initial cathodic scan correspond to the generation of $Li_xCu_{3-x}P$,[21,22,25,29,45] and a reduction peak below 0.14 V corresponds to the formation of Cu and Li_3P.[46,47] The reduction peaks shift toward the high voltage region owing to the generation of superfine Cu_3P nanoparticles with increased reaction activity (see Fig. S6† and the below mechanism study).[25] In the anodic scans, two weak oxidation peaks near 0.83 and 1.32 V and a strong oxidation peak near 1.21 V can be ascribed to the reversible delithiation process accompanied by the generation of $Li_{3-x}Cu_x$-P.[21,22,25,29,45–47] Remarkably, no obvious oxidation peak near 2.5 V corresponding to the oxidation of Cu into CuO was observed, suggesting a negligible content of CuO in the Cu_3P@C–Cu electrode. The CV curves are in accordance with the charge/discharge curves in Fig. S7.†

The capacity variation of the Cu_3P@C correlates well with the electrochemical reconstruction process.[48–50] As shown in Fig. 5b, the increase in capacity suggests an enhanced Li storage owing to the refinement of Cu_3P particles and the spread of coated C, and a high discharge/charge capacity of 418/415 mA h g^{-1} can be achieved after 500 cycles. Such capacity variation is accompanied by a high average coulombic efficiency of 98.5%. An electrochemical reconstruction induced capacity increase was also found when cycling at 0.1 A g^{-1} (Fig. S8†). Furthermore, the charge transfer resistance (R_{ct}) of the Cu_3P@C reduces in the first few cycles from 124.3 to 81.3 Ω, and then stabilizes at ~58 Ω

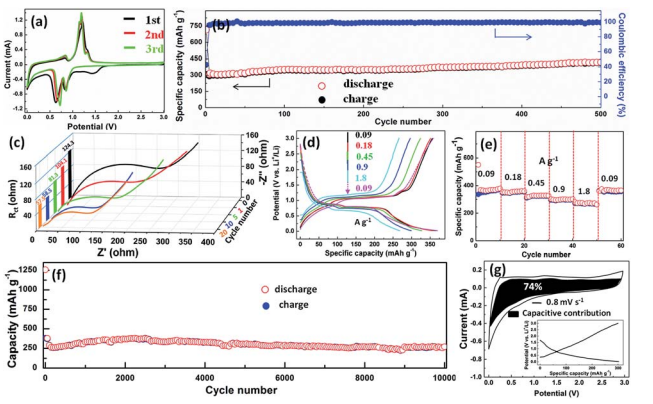

Fig. 5 The electrochemical performance of the Cu_3P@C–Cu electrode. (a) The initial three CV curves. (b) Capacity retention and coulombic efficiency at 0.15 A g^{-1}. (c) EIS spectra at different stages. (d) Representative charge/discharge curves and (e) capacity retention at various currents. (f) Long-time performance at 4.2 A g^{-1} (10 cycles with activation at 0.42 A g^{-1}). (g) Capacitive contribution to charge storage at 0.6 mV s^{-1} after 5000 cycles at 4.2 A g^{-1}. The inset of (g) is the 5000th charge/discharge curve.

Table 1 The summary of the electrochemical performance of various Cu_3P electrodes

Electrode	Current 1C ≈360 mA g^{-1}	Lifespan	Attenuation per cycle	Ref.
Cu_3P	C/20	10	6.19%	22
Cu_3P–Cu	C/20	13	4.00%	23
Cu_3P–Cu	0.3C	70	−0.047%	25
Cu_3P	∼1.4C	80	0.74%	26
Cu_3P	0.5C	50	1.27%	27
Cu_3P	C/20	21	1.31%	28
Cu_3P	C/8	16	1.17%	29
Cu_3P	C/70	20	1.28%	45
Cu_3P	0.1C	20	2.62%	53
Cu_3P	0.2C	50	0.94%	54
Cu_3P@C–Cu	∼0.4C	500	−0.032%	This work
	∼5C	10 000	0.027%	

after 10 cycles (Fig. 5c), suggesting enhanced electronic conductivity accompanied by the formation of the D-in-M architecture. Based on the self-adaptive electrochemical properties in terms of the reaction activity and R_{ct}, the electrochemical performance of the Cu_3P@C–Cu electrode was evaluated. As seen, the Cu_3P@C shows low voltage polarization from 0.09 to 1.8 A g^{-1} (Fig. 5d),[51,52] and delivers a high capacity recovery of 375 mA h g^{-1}. More impressive is the superior high-rate performance. As shown in Fig. 5f, even after 10 000 cycles at 4.2 A g^{-1}, the Cu_3P@C can deliver a charge/discharge capacity of 270/269 mA h g^{-1}. As seen in the comprehensive survey in Table 1, both the lifespan and capacity retention of the Cu_3P@C show a distinct improvement compared to the reported Cu_3P-related electrodes.[22,23,25–29,45,53,54] The Cu_3P@C also delivers a much longer lifespan than that of Co_2P, $Ni_{12}P_5$, Ni_2P, Zn_3P_2 and GeP.[55–59] Apart from the significantly improved lifespan under a constant current, the Cu_3P@C also delivers stable cycling under an irregularly varied current (Fig. S9†). Fast reaction kinetics were also triggered by the self-adaptive electrochemical reconstruction. As shown in Fig. 5g, typical capacitive characteristics of the cycled electrode can be observed from the CV and charge/discharge curves. According to the equation $i(V) = k_1v + k_2v^{1/2}$, the capacitive contribution to the charge storage can be extracted by separating the k_1v part,[60–62] where k_1 is constant and can be determined by the CV curves at different scan rates (Fig. S10†).[63] The cycled Cu_3P@C–Cu electrode exhibits a high capacitive contribution of 74%, demonstrating fast reaction kinetics induced by self-adaptive electrochemical reconstruction, boosting the superior high-rate performance.[62,64] Taking into consideration the low and safe lithiation/delithiation potential (*vs.* graphite) and the high specific capacity of Cu_3P (*vs.* $Li_4Ti_5O_{12}$), the practical applications of Cu_3P in full cells are of great appeal. When matched with a commercial $LiFePO_4$ cathode, the full cell exhibits a distinct discharge plateau near 2.2–2.3 V and a charge plateau near 2.5–2.6 V as well as stable cycling (Fig. S11†), demonstrating the great potential of Cu_3P anodes for commercialization.

Conclusions

The triggering of exceptional performance of conversion anode materials *via* a self-adaptive electrochemical reconstruction is demonstrated, in the case of Cu_3P, a typical anode material with pretty good charge/discharge plateaus but moderate performance. By tracking the morphology and microstructure variation upon cycling and the related electrochemical properties, it is found that Cu_3P@C dramatically evolves into well dispersed Cu_3P dots embedded in a carbon matrix *via* a self-adaptive electrochemical reconstruction, which gives high Li-ion storage activity, improved electronic conductivity and stability. All of these, together, trigger exceptional performance. As a result, the designed Cu_3P@C–Cu electrode delivers the longest lifespan compared to all of the Cu_3P electrodes ever reported up to now. Specifically, it exhibits no capacity fading at 0.15 A g^{-1} up to 500 cycles and little capacity fading at 4.2 A g^{-1} over 10 000 cycles. These values are among the best for Cu_3P-based anodes. Our results highlight the importance of electrochemical reconstruction in boosting electrochemical performance, and open new ideas for high-performance conversion anode design.

Conflicts of interest

There are no conflicts to declare.

Acknowledgements

Prof. Shibing Ni acknowledges financial support from the National Natural Science Foundation of China (NSFC, 51672158) and the open project of the State Key Laboratory of Physical Chemistry of Solid Surfaces (201608). Prof. Zexiang Shen acknowledges financial support from the Ministry of Education, Tier 1 (Grant number: M4011424.110) and Tier 2 (Grant number: M4020284.110).

Notes and references

1 P. Poizot, S. Laruelle, S. Grugeon, L. Dupont and J. M. Tarascon, *Nature*, 2000, **407**, 496–499.
2 A. S. Arico, P. Bruce, B. Scrosati, J. M. Tarascon and W. V. Schalkwijk, *Nat. Mater.*, 2005, **4**, 366–377.
3 L. W. Ji, Z. Lin, M. Alcoutlabi and X. W. Zhang, *Energy Environ. Sci.*, 2011, **4**, 2682–2699.

4 J. M. Jeong, B. G. Choi, S. C. Lee, K. G. Lee, S. J. Chang, Y. K. Han, Y. B. Lee, H. U. Lee, S. Kwon, G. Lee, C. S. Lee and Y. S. Huh, *Adv. Mater.*, 2013, **25**, 6250–6255.
5 J. S. Cho, Y. J. Hong and Y. C. Kang, *ACS Nano*, 2015, **9**, 4026–4035.
6 Y. Kim, J. H. Lee, S. Cho, Y. Kwon, I. In, J. Lee, N. H. You, E. Reichmanis, H. Ko, K. T. Lee, H. K. Kwon, D. H. Ko, H. Yang and B. Park, *ACS Nano*, 2014, **8**, 6701–6712.
7 X. L. Sun, C. L. Yan, Y. Chen, W. P. Si, J. W. Deng, S. Oswald, L. F. Liu and O. G. Schmidt, *Adv. Energy Mater.*, 2014, **4**, 1300912.
8 R. Dang, X. L. Jia, X. Liu, H. T. Ma, H. Y. Gao and G. Wang, *Nano Energy*, 2017, **33**, 427–435.
9 W. M. Zhang, X. L. Wu, J. S. Hu, Y. G. Guo and L. J. Wan, *Adv. Funct. Mater.*, 2008, **18**, 3941–3946.
10 H. W. Zhang, L. Zhou, O. Noonan, D. J. Martin, A. K. Whittaker and C. Z. Yu, *Adv. Funct. Mater.*, 2014, **24**, 4337–4342.
11 Y. Wu, Y. Wei, J. P. Wang, K. L. Jiang and S. S. Fan, *Nano Lett.*, 2013, **13**, 818–823.
12 C. N. He, S. Wu, N. Q. Zhao, C. S. Shi, E. Z. Liu and J. J. Li, *ACS Nano*, 2013, **7**, 4459–4469.
13 C. X. Peng, B. D. Chen, Y. Qin, S. H. Yang, C. Z. Li, Y. H. Zuo, S. Y. Liu and J. H. Yang, *ACS Nano*, 2012, **6**, 1074–1081.
14 J. Liang, H. Hu, H. J. Park, C. H. Xiao, S. J. Ding, U. Paikc and X. W. Lou, *Energy Environ. Sci.*, 2015, **8**, 1707–1711.
15 P. L. Taberna, S. Mitra, P. Poizot, P. Simon and J. M. Tarascon, *Nat. Mater.*, 2006, **5**, 567–573.
16 J. S. Luo, J. L. Liu, Z. Y. Zeng, C. F. Ng, L. J. Ma, H. Zhang, J. Y. Lin, Z. X. Shen and H. J. Fan, *Nano Lett.*, 2013, **13**, 6136–6143.
17 X. L. Huang, R. Z. Wang, D. Xu, Z. L. Wang, H. G. Wang, J. J. Xu, Z. Wu, Q. C. Liu, Y. Zhang and X. B. Zhang, *Adv. Funct. Mater.*, 2013, **23**, 4345–4353.
18 X. L. Sun, W. P. Si, X. H. Liu, J. W. Deng, L. X. Xi, L. F. Liu, C. L. Yan and O. G. Schmidt, *Nano Energy*, 2014, **9**, 168–175.
19 J. X. Wang, Q. B. Zhang, X. H. Li, D. G. Xu, Z. X. Wang, H. J. Guo and K. L. Zhang, *Nano Energy*, 2014, **6**, 19–26.
20 S. B. Ni, P. Huang, D. L. Chao, G. D. Yuan, L. C. Zhang, F. Z. Zhao and J. M. Li, *Adv. Funct. Mater.*, 2017, **27**, 1701808.
21 C. Villevieille, F. Robert, P. L. Taberna, L. Bazin, P. Simon and L. Monconduit, *J. Mater. Chem.*, 2008, **18**, 5956–5960.
22 H. Pfeiffer, F. Tancret and T. Brousse, *Electrochim. Acta*, 2005, **50**, 4763–4770.
23 H. Pfeiffer, F. Tancret, M. P. Bichat, L. Monconduit, F. Favier and T. Brousse, *Electrochem. Commun.*, 2004, **6**, 263–267.
24 M. S. Chandrasekar and S. Mitra, *Electrochim. Acta*, 2013, **92**, 47–54.
25 S. B. Ni, J. J. Ma, X. H. Lv, X. L. Yang and L. L. Zhang, *J. Mater. Chem. A*, 2014, **2**, 20506–20509.
26 S. L. Liu, X. D. He, J. P. Zhu, L. Q. Xu and J. B. Tong, *Sci. Rep.*, 2016, **6**, 35189.
27 A. J. Zhou, B. Yang, W. H. Wang, X. Y. Dai, M. J. Zhao, J. Xue, M. G. Han, C. Fan and J. Z. Li, *RSC Adv.*, 2016, **6**, 26800–26808.
28 M. P. Bichat, T. Politova, H. Pfeiffer, F. Tancret, L. Monconduit, J. L. Pascal, T. Brousse and F. Favier, *J. Power Sources*, 2014, **136**, 80–87.
29 M. P. Bichat, T. Politova, J. L. Pascal, F. Favier and L. Monconduit, *J. Electrochem. Soc.*, 2004, **151**, A2074–A2081.
30 J. L. Zhu, Q. L. Wu, J. Key, M. M. Wu and P. K. Shen, *Energy Storage Mater.*, 2018, **15**, 75–81.
31 X. He, R. Wang, M. C. Stan, E. Paillard, J. Wang, H. Frielinghaus and J. Li, *Adv. Mater. Interfaces*, 2017, **4**, 1601047.
32 S. L. Liu, C. Liu, J. Guo and W. Yan, *J. Electrochem. Soc.*, 2017, **164**, A2390–A2397.
33 Z. L. Jian, M. B. Zheng, Y. L. Liang, X. X. Zhang, S. Gheytani, Y. C. Lan, Y. Shi and Y. Yao, *Chem. Commun.*, 2015, **51**, 229–231.
34 C. K. Zhang, H. Q. Song, C. F. Liu, Y. G. Liu, C. P. Zhang, X. H. Nan and G. Z. Cao, *Adv. Funct. Mater.*, 2015, **25**, 3497–3504.
35 S. B. Ni, J. C. Zhang, J. J. Ma, X. L. Yang and L. L. Zhang, *J. Mater. Chem. A*, 2015, **3**, 17951–17955.
36 M. P. Fan, Y. Chen, Y. H. Xie, T. Z. Yang, X. W. Shen, N. Xu, H. Y. Yu and C. L. Yan, *Adv. Funct. Mater.*, 2016, **26**, 5019–5027.
37 J. H. Hao, W. S. Yang, Z. P. Huang and C. Zhang, *Adv. Mater. Interfaces*, 2016, **3**, 1600236.
38 J. Q. Tian, Q. Liu, N. Y. Cheng, A. M. Asiri and X. P. Sun, *Angew. Chem., Int. Ed.*, 2014, **126**, 9731–9735.
39 Y. Qiao, X. L. Hu, Y. Liu, C. J. Chen, H. H. Xu, D. F. Hou, P. Hu and Y. H. Huang, *J. Mater. Chem. A*, 2013, **1**, 10375–10381.
40 Y. Lu, X. L. Wang, Y. J. Mai, J. Y. Xiang, H. Zhang, L. Li, C. D. Gu, J. P. Tu and S. X. Mao, *J. Phys. Chem. C*, 2012, **116**, 22217–22225.
41 C. C. Kong, L. L. Tang, X. Z. Zhang, S. D. Sun, S. C. Yang, X. P. Song and Z. M. Yang, *J. Mater. Chem. A*, 2014, **2**, 7306–7312.
42 M. Durando, R. Morrish and A. J. Muscat, *J. Am. Chem. Soc.*, 2008, **130**, 16659–16668.
43 S. B. Ni, J. C. Zhang, J. J. Ma, X. L. Yang, L. L. Zhang, X. M. Li and H. B. Zeng, *Adv. Mater. Interfaces*, 2016, **3**, 1500340.
44 H. Kim, M. Seo, M. H. Park and J. A. Cho, *Angew. Chem., Int. Ed.*, 2010, **49**, 2146–2149.
45 B. Mauvernay, M. P. Bichat, F. Favier, L. Monconduit, M. Morcrette and M. L. Doublet, *Ionics*, 2005, **11**, 36–45.
46 F. Poli, J. S. Kshetrimayum, L. Monconduit and M. Letellier, *Electrochem. Commun.*, 2011, **13**, 1293–1295.
47 F. Poli, A. Wong, J. S. Kshetrimayum, L. Monconduit and M. Letellier, *Chem. Mater.*, 2016, **28**, 1787–1793.
48 S. B. Ni, X. H. Lv, T. Li, X. L. Yang, L. L. Zhang and Y. Ren, *Electrochim. Acta*, 2013, **96**, 253–260.
49 Y. M. Sun, X. L. Hu, W. Luo, F. F. Xia and Y. H. Huang, *Adv. Funct. Mater.*, 2013, **23**, 2436–2444.
50 S. B. Ni, J. J. Ma, J. C. Zhang, X. L. Yang and L. L. Zhang, *Chem. Commun.*, 2015, **51**, 5880–5882.
51 B. Varghese, M. V. Reddy, Z. Yanwu, C. S. Lit, T. C. Hoong, G. V. S. Rao, B. V. R. Chowdari, A. T. S. Wee, C. T. Lim and C. H. Sow, *Chem. Mater.*, 2008, **20**, 3360–3367.
52 X. H. Wang, X. W. Li, X. L. Sun, F. Li, Q. M. Liu, Q. Wang and D. Y. He, *J. Mater. Chem.*, 2011, **21**, 3571–3573.

53 S. L. Liu, S. Li, J. P. Wang, Q. Q. Shi and M. M. Li, *Mater. Res. Bull.*, 2012, **47**, 3352–3356.
54 M. C. Stan, R. Klöpsch, A. Bhaskar, J. Li, S. Passerini and M. Winter, *Adv. Energy Mater.*, 2013, **3**, 231–238.
55 D. Yang, J. X. Zhu, X. H. Rui, H. T. Tan, R. Cai, H. E. Hoster, D. Y. W. Yu, H. H. Hng and Q. Y. Yan, *ACS Appl. Mater. Interfaces*, 2013, **5**, 1093–1099.
56 H. J. Zhang, Y. Y. Feng, Y. Zhang, L. Fang, W. X. Li, Q. Liu, K. Wu and Y. Wang, *ChemSusChem*, 2014, **7**, 2000–2006.
57 S. Carenco, C. Surcin, M. Morcrette, D. Larcher, N. Mézailles, C. Boissière and C. Sanchez, *Chem. Mater.*, 2014, **24**, 688–697.
58 W. W. Li, L. Gan, K. Guo, L. B. Ke, Y. Q. Wei, H. Q. Li, G. Z. Shen and T. Y. Zhai, *Nanoscale*, 2016, **8**, 8666–8672.
59 W. W. Li, H. Q. Li, Z. J. Lu, L. Gan, L. B. Ke, T. Y. Zhai and H. S. Zhou, *Energy Environ. Sci.*, 2015, **8**, 3629–3636.
60 J. L. Liu, J. Wang, C. H. Xu, H. Jiang, C. Z. Li, L. L. Zhang, J. Y. Lin and Z. X. Shen, *Adv. Sci.*, 2018, **5**, 1700322.
61 T. Brezesinski, J. Wang, S. H. Tolbert and B. Dunn, *Nat. Mater.*, 2010, **9**, 146–151.
62 V. Augustyn, J. Come, M. A. Lowe, J. W. Kim, P. L. Taberna, S. H. Tolbert, H. D. Abruña, P. Simon and B. Dunn, *Nat. Mater.*, 2013, **12**, 518–522.
63 D. L. Chao, C. R. Zhu, P. H. Yang, X. H. Xia, J. L. Liu, J. Wang, X. F. Fan, S. V. Savilov, J. Y. Lin, H. J. Fan and Z. X. Shen, *Nat. Commun.*, 2016, **7**, 12122.
64 J. Wang, J. Polleux, J. Lim and B. Dunn, *J. Phys. Chem. C*, 2007, **111**, 14925–14931.